

Article

Growth of Catalyst-Free Hexagonal Pyramid-Like InN Nanocolumns on Nitrided Si(111) Substrates via Radio-Frequency Metal–Organic Molecular Beam Epitaxy

Wei-Chun Chen ^{1,*} , Tung-Yuan Yu ², Fang-I Lai ³, Hung-Pin Chen ¹, Yu-Wei Lin ¹ and Shou-Yi Kuo ^{4,5,*} 

¹ Taiwan Instrument Research Institute, National Applied Research Laboratories, 20, R&D Rd. VI, Hsinchu Science Park, Hsinchu 30076, Taiwan; chbin@tiri.narl.org.tw (H.-P.C.); james722@tiri.narl.org.tw (Y.-W.L.)

² Taiwan Semiconductor Research Institute, National Applied Research Laboratories, 26, Prosperity Road I, Hsinchu Science Park, Hsinchu 30078, Taiwan; tyuu@tsri.narl.org.tw

³ Electrical Engineering Program C, Yuan-Ze University, 135 Yuan-Tung Road, Chung-Li 32003, Taiwan; filai@saturn.yzu.edu.tw

⁴ Department of Electronic Engineering, Chang Gung University, 259 Wen-Hwa 1st Road, Kwei-Shan, Taoyuan 33302, Taiwan

⁵ Department of Urology, Chang Gung Memorial Hospital, Linkou, No.5, Fuxing Street, Kwei-Shan, Taoyuan 333, Taiwan

* Correspondence: weichun@narlabs.org.tw (W.-C.C.); sykuo@mail.cgu.edu.tw (S.-Y.K.); Tel.: +886-3577-9911 (ext. 646) (W.-C.C.); +886-3211-8800 (ext. 3351) (S.-Y.K.)

Received: 1 May 2019; Accepted: 3 June 2019; Published: 5 June 2019



Abstract: Hexagonal pyramid-like InN nanocolumns were grown on Si(111) substrates via radio-frequency (RF) metal–organic molecular beam epitaxy (MOMBE) together with a substrate nitridation process. The metal–organic precursor served as a group-III source for the growth of InN nanocolumns. The nitridation of Si(111) under flowing N₂ RF plasma and the MOMBE growth of InN nanocolumns on the nitrided Si(111) substrates were investigated along with the effects of growth temperature on the structural, optical, and chemical properties of the InN nanocolumns. Based on X-ray diffraction analysis, highly <0001>-oriented, hexagonal InN nanocolumns were grown on the nitride Si(111) substrates. To evaluate the alignment of arrays, the deviation angles of the InN nanocolumns were measured using scanning electron microscopy. Transmission electron microscopy analysis indicated that the InN nanocolumns were single-phase wurtzite crystals having preferred orientations along the *c*-axis. Raman spectroscopy confirmed the hexagonal structures of the deposited InN nanocolumns.

Keywords: InN nanocolumns; nitridation; nitrided Si(111)

1. Introduction

Nanocolumns (NCs) have proven effective for lateral stress relaxation; thus, they exhibit low defect densities in III-nitride heterostructures. This property is particularly beneficial for systems with large lattice mismatch, such as indium nitride (InN), which is typically grown on foreign substrates. InN is an interesting and potentially important III-nitride semiconductor material with superior electronic transport properties [1]. InN has attracted considerable research attention concerning the development of optoelectronic devices (e.g., full-color light-emitting diodes, solar cells, and optochemical sensors [2]) because of its room temperature direct optical band gap in the near-infrared region ($E_g = 0.7$ eV) [3]. Moreover, the electron mobility of InN can exceed 2100 cm²/(V·s) with a residual carrier concentration

approaching $8 \times 10^{17} \text{ cm}^{-3}$ at room temperature [4]. However, the relatively low decomposition temperature ($<600 \text{ }^\circ\text{C}$) in the III-nitride materials [5], large lattice mismatch with universal substrates, and impurity-prone surface of InN hinder the development of InN-related devices. Furthermore, the narrow growth window of InN (between $500 \text{ }^\circ\text{C}$ and $550 \text{ }^\circ\text{C}$) limits device processing. InN nanocolumns have been grown on Si(111) substrates with buffer layers such as Si_3N_4 [6], GaN, low-temperature InN [7], AlN/ Si_3N_4 double-layers [8], InN/ Si_3N_4 double-layers [9], and InGaN [10].

Al_2O_3 has been widely used as a substrate for heteroepitaxial InN growth despite its insulating property and large a -axis lattice mismatch with InN ($\sim 25\%$). Si(111) is a more suitable substrate for InN growth because it has a smaller lattice mismatch with InN ($\sim 8\%$), better doping properties, and greater thermal conductivity compared to Al_2O_3 . $\beta\text{-Si}_3\text{N}_4$ has a lattice constant of 7.602 \AA along its a -axis [11], which is only slightly larger than twice the lattice constant of InN ($a = 3.548 \text{ \AA}$). If twice the lattice constant of InN is considered a nominal lattice constant, the lattice mismatch between Si and InN will be small.

InN nanocolumns have been grown using various methods, including radio-frequency (RF) molecular beam epitaxy (MBE) [12], RF sputtering [13], and metal-organic chemical vapor deposition (MOCVD) [14]. However, because of the low dissociation efficiency of ammonia, these methods require large amounts of ammonia to obtain the flux of active nitrogen required for producing high-quality nitride. Although substantial progress has been made in the development of plasma sources to mitigate this nitrogen problem, the InN growth rates of the above methods are still lower than that achieved via metal-organic molecular beam epitaxy (MOCVD). RF-MOMBE, which is performed in a growth chamber with a load lock and a base pressure of $\sim 10^{-9}$ Torr, combines the characteristics of both MBE and MOCVD and is suitable for the mass production of InN. In the RF-MOMBE growth of InN, a precursor such as trimethylaluminum or trimethylindium (TMIn) serves as the group-III precursor, and atomic nitrogen generated by RF plasma is the source of N. Due to low dissociation temperature and high N_2 equilibrium pressure over InN, plasma-assisted systems are thought to be suitable for InN growth. Compared to the MOCVD growth of epitaxial nitride films, RF-MOMBE generally allows for a lower growth temperature [15]. In our previous study, the RF-MOMBE growth temperatures of InN-related alloys were all lower than the corresponding MOCVD growth temperatures [16]. Despite the promising characteristics of RF-MOMBE, few studies have reported the RF-MOMBE growth of hexagonal pyramid-like InN nanocolumns. Therefore, in this study, we focused on nitride growth at low temperature, including AlN growth at $800\text{--}900 \text{ }^\circ\text{C}$, InN growth at $450\text{--}550 \text{ }^\circ\text{C}$, and GaN growth at $750\text{--}850 \text{ }^\circ\text{C}$.

According to previous studies, InN materials grown via RF-MOMBE have often been deposited on sapphire substrates. Silicon (Si) is a promising material for the growth of group-III-V materials. The good thermal conductivity of Si is especially interesting for electronic applications, including low-cost, high-brightness light-emitting diodes, and high-power chips. However, few studies have grown InN nanostructures on Si(111) substrates via RF-MOMBE. Nitride thin films could be suitable buffer layers for the growth of InN on Si wafers and other lattice-mismatched group-III-V heteroepitaxial systems.

Previous studies have shown that InN grown on nitrated Si(111) substrates exhibits good crystallinity. Kumar et al. reported that InN films deposited onto Si substrates with different buffer layers exhibited high crystallinity and wurtzite lattice structures; furthermore, the InN/ Si_3N_4 double buffer layer exhibited a minimum full-width at half-maximum (FWHM) of the $E_2(\text{high})$ mode [9]. Segura-Ruiz et al. [17] reported the growth of misoriented and tilted InN nanorods on Si(111) substrates with amorphous Si_xN_y buffer layers. However, Park et al. [18] reported the deposition of porous Si_xN_y buffer layers with numerous nanometer-sized holes under certain experimental conditions; such a porous buffer layer could be a good template for the low-temperature deposition of nitride layers. Nishikawa et al. [19] reported that both substrate nitridation and growth initiation via In droplet formation are essential for the growth of InN nanocolumns with excellent c -axis orientation. InN nanostructures such as nanowires, nanotubes, and nanocolumns have attracted considerable attention because the

quantum confinement effect may yield novel functions and improved performance [20]. Lee et al. [21] reported the predeposition of In before the growth of InN nanocolumns; InN nanocolumns were obtained by forming droplets of Au + In solid solution on Au-coated substrates following by nitriding these droplets.

In this study, hexagonal pyramid-like InN nanocolumns were grown on nitrided Si(111) substrates via catalyst-free RF-MOMBE in conjunction with substrate nitridation. The substrate was nitrided at 900 °C for 60 min. InN nanocolumns were subsequently grown on the nitrided Si(111) substrate at 500–540 °C. The effects of growth temperature on the structural, optical, and electrical properties of the InN nanocolumns were then investigated.

2. Materials and Methods

InN nanocolumns were grown on nitrided mirror-like Si(111) wafers as substrates. The growth chamber was evacuated to a base pressure of 10^{-9} Torr using a turbomolecular pump. TMIIn, which served as the group-III precursor, was delivered to the growth chamber by heating the metal–organic source in the absence of a carrier gas. Active nitrogen radicals were supplied by a RF plasma source (13.56 MHz). The Si(111) wafers were cleaned on a wet bench using the standard Radio Corporation of America process. The wafers were then dipped in buffered oxide etching solution for 5 min to remove native surface oxides. Subsequently, the substrates were placed in the growth chamber and thermally cleaned at 900 °C for 90 min under ultrahigh vacuum to remove any oxide residues in preparation for nitridation and InN growth.

The Si(111) substrates were nitrided at 900 °C for 60 min and then cooled to 500–540 °C for InN growth. The N_2 (99.9999%) flow rate was 1 sccm, and the RF plasma power was 300 W. The dynamic pressure of the growth chamber during deposition was approximately 2×10^{-5} Torr.

The structural properties of the InN nanocolumns were characterized by X-ray diffraction (XRD; Bruker D8 ADVANCE, AXS GmbH, Karlsruhe, Germany) with a Cu-K α X-ray source. The surface morphologies of the InN nanocolumns were examined by field-emission scanning electron microscopy (FE-SEM; Hitachi S-4300 FE-SEM, Hitachi, Ltd, Chiyoda-ku, Japan), while the InN microstructure was analyzed by field-emission transmission electron microscopy (FE-TEM; JEOL ARM200F, JEOL Ltd, Toyoko, Japan) with an electron voltage of 200 kV. Cross-sectional TEM specimens were prepared using a dual-beam focused ion beam (Seiko SII-3050; manufactured by FEI, Hillsboro, OR, USA). Raman spectroscopy (HR800; Horiba Jobin Yvon Labram, Bensheim, Germany) was performed at room temperature in backscattering geometry using the 514.5-nm Ar⁺ laser line for excitation. X-ray photoelectron spectroscopy (VG ESCA/XPS Theta Probe; Thermo Fisher Scientific Inc., Waltham, MA, USA) with Al K α ($h\nu = 1486.6$ eV) radiation was used to characterize the bonding characteristics of the elements in the films.

3. Results and Discussion

Figure 1 shows the XRD patterns of the InN nanocolumns grown at various temperatures on the nitrided Si(111) substrates. All patterns show the peaks of Si(111) ($2\theta = 28.44^\circ$) and Si(222) ($2\theta = 58.86^\circ$), a strong InN(0002) peak ($2\theta = 31.36^\circ$), a weak InN(10–13) peak ($2\theta = 56.9^\circ$), and the InN(0004) peak ($2\theta = 65.4^\circ$). The XRD results indicate the formation of highly <0001>-oriented hexagonal InN nanocolumns on the nitrided Si(111) substrates, similar to the results of Feng et al. [6]. The peaks at $2\theta = 44.1^\circ$ and 64.4° are attributed to the XRD sample stage.

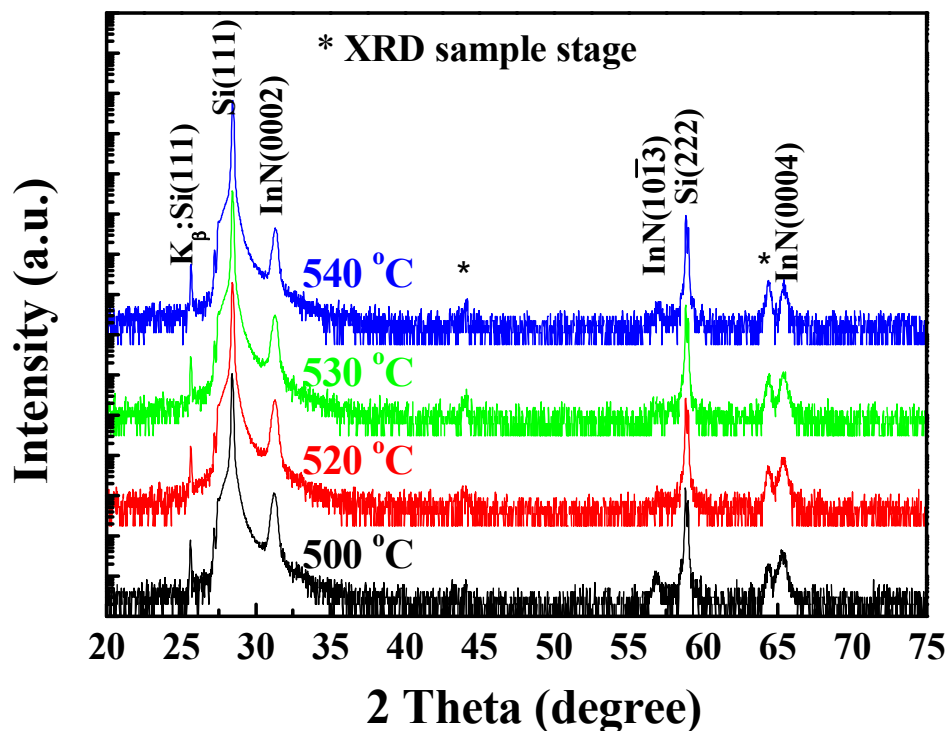


Figure 1. X-ray diffraction (XRD) θ – 2θ diffraction patterns of InN grown on nitrided Si(111) substrates at different temperatures from 500 °C to 540 °C.

The *c*-axis lattice parameter of the InN nanocolumns was calculated to be approximately 0.57 nm, in agreement with the value reported for InN bulk crystal [22]. The results indicate stress relaxation in the InN nanocolumns after growth. The FWHM values of the XRD peaks were determined from the ω scans of the InN(0002) reflection (results not shown). The FWHM values of the samples grown at 500 °C, 520 °C, 530 °C, and 540 °C were approximately 366, 360, 389, and 480 arcmin, respectively, indicating that the broad peaks can be attributed to the high defect densities and amorphous In–O compounds in the InN nanocolumns. The crystalline quality was slightly better in the InN nanocolumns grown at 520 °C compared to those grown at 500 °C, implying that the growth temperature was within the reactive regime.

Figure 2 presents SEM micrographs showing the surface morphologies and cross-sections of the InN nanocolumns. All of the InN nanocolumns grew preferentially along the $\langle 0001 \rangle$ direction. Growth began from a thin polycrystalline InN nucleation layer on top of the nitrided Si₃N₄ ultrathin buffer layer. These results reflect the fact that the InN nanocolumns were grown via chemical reaction from TMIn and RF N₂ plasma. The average growth rate of the InN nanocolumns was approximately 0.8 $\mu\text{m}/\text{h}$. The InN growth rate achieved by RF-MOMBE is higher than that of conventional MBE. In this study, the InN nanocolumns exhibited three-dimensional (3D) features with varying nanometer-scale structures and shapes ranging from pyramid-like columns to pyramids depending on growth temperature. The plane-view SEM images show that aligned, self-assembled InN nanocolumns with diameters of 60 to 120 nm formed uniformly over the entire substrate at a high density of approximately 10^{10} cm^{-2} at growth temperatures of 500 to 540 °C. The densities of InN nanocolumns grown at 500 °C, 520 °C, 530 °C, and 540 °C were approximately $5.3 \times 10^{10} \text{ cm}^{-2}$, $4.8 \times 10^{10} \text{ cm}^{-2}$, $3.7 \times 10^{10} \text{ cm}^{-2}$, and $1.3 \times 10^{10} \text{ cm}^{-2}$, respectively. Thus, the density decreased with increasing growth temperature. The density, size, and shape of the InN nanocolumns were mainly determined by the diffusion of In adatoms. During the initial stages of the growth process, the formation of TMIn and/or In droplets enhanced nucleation at specific locations, resulting in columnar growth [23]. Thus, since the diffusion of In increases with temperature, the density of InN nuclei was insufficient for columnar growth at high temperature. The large column diameter can likely be attributed to the large seed size and low density of nuclei during

the initial growth stage at high growth temperature, which gave rise to a high lateral growth rate and cracking of the TMIn precursor (i.e., reaction of TMIn with nitrogen), leading to large grain size. The typical nanocolumn height was approximately 240 nm. The nanocolumn diameter increased from 60 to 130 nm as the growth temperature was increased from 500 °C to 540 °C. The InN nanocolumns grown at 500 °C and 520 °C were similar in size. Some of the nanocolumns were oriented along the *c*-axis without tapering, whereas others were tilted with respect to the substrate normal. When the growth temperature was further increased, nanocolumns with diameters and heights of approximately 80 and 220 nm (530 °C) or 130 nm and 240 nm (540 °C), respectively, were observed. The deviation angles of the InN nanocolumns grown at 500 °C, 520 °C, and 530 °C were determined to be 75°, 75°, and 80°, respectively. The height:diameter (*h/d*) ratio of the nanocolumns decreased as the growth temperature increased to 540 °C. The growth temperature was shown to affect the diffusion of In adatoms along nanorod sidewalls [16]. Since the In diffusion length increases with temperature, high temperature leads to the decomposition of In–N. In our previous study, continuous InN films were grown via RF-MOMBE at various temperatures in the range of 500–540 °C. Therefore, the above results demonstrate that the size, morphology, and optimal growth temperature of InN nanocolumns were influenced by the nitrided Si(111) substrate. The results are similar to those observed for InN nanorods grown via MBE [24].

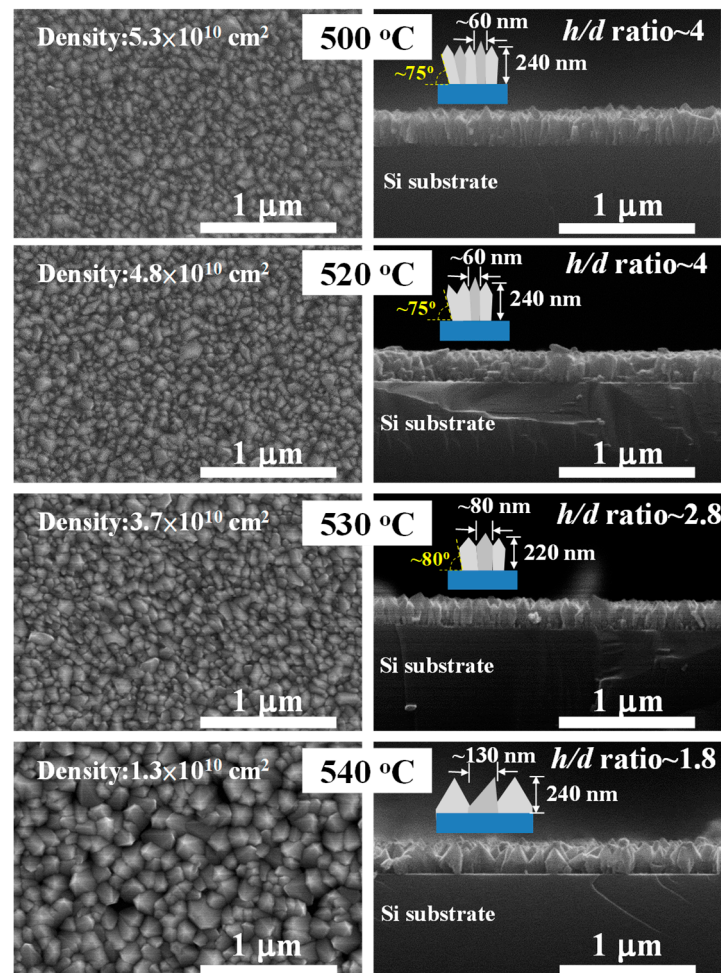


Figure 2. Plane-view and cross-sectional SEM images of InN grown on nitrided Si(111) substrates at different temperatures in the range of 500 to 540 °C.

TEM was used to characterize the microstructures of the InN nanocolumns and nitrided Si_xN_y. Cross-sectional TEM specimens were prepared from the grown layers. The dark-field TEM image of

a nitrided Si_xN_y ultra layer (Figure 3a) clearly shows a rough surface, which was likely caused by plasma-beam damage to the $\text{Si}_x\text{N}_y/\text{Si}(111)$ surface. The observed V-like holes are consistent with the N_2 plasma-beam damaging a nonstoichiometric silicon nitride layer [25]. Figure 3b shows a cross-sectional bright-field TEM (XTEM) image of InN nanocolumns grown on a nitrided Si(111) substrate at 520 °C. The electron beam incident direction in Figure 3b is parallel to the $[\bar{1}120]_{\text{InN}}$ direction, while the vertical axis is parallel to the $[0001]_{\text{InN}}$ direction. Similar to the SEM results, the XTEM images indicate a rough InN surface and V-like holes in the interface between InN and the Si substrate. For InN nanocolumns grown on the V-like holes, the crystals likely grew along the sidewalls of the holes, resulting in a deviation in growth angle. As a result, the initial growth of adjacent InN nanocolumns occurred in the voids between the substrate and InN nanocolumns. A previous study found that amorphous Si_xN_y can develop gradually on bare Si(111) before the growth of InN [26]. Thus, the epitaxial relation is lost on the nitrided area, resulting in misoriented nanorods or a coarse-grained structure on Si(111).

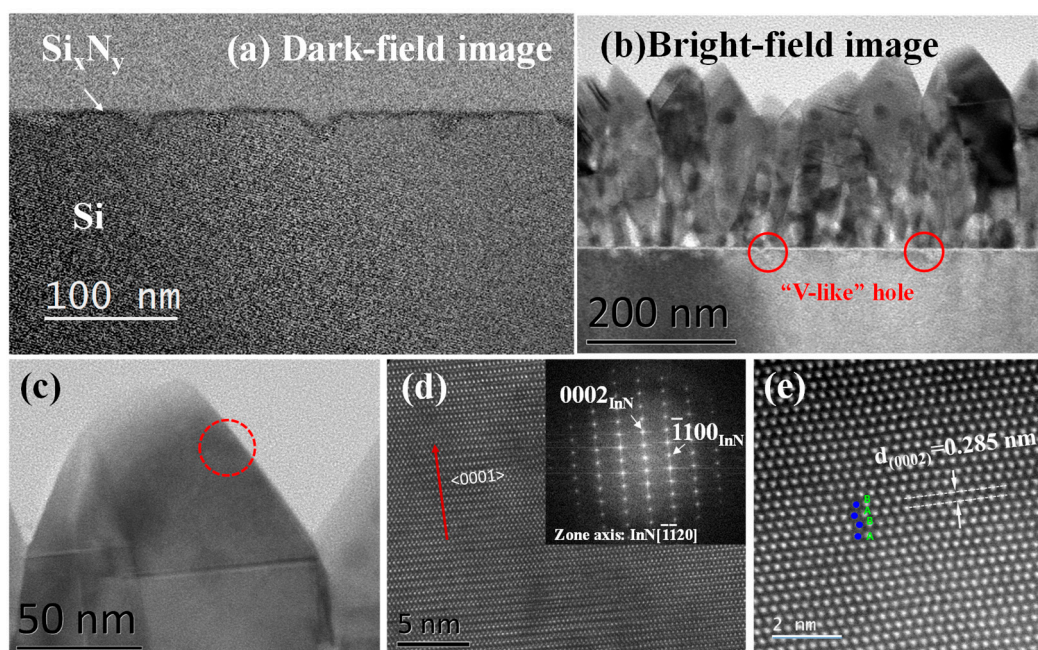


Figure 3. (a) Cross-sectional bright-field TEM (XTEM) image of nitrided Si(111). (b) XTEM image of InN nanocolumns grown on a nitrided Si(111) substrate. (c) XTEM image of the top of a InN nanocolumn. (d) High-resolution scanning electron microscopy (HRTEM) image of the area in c indicated by the red dashed circle. The inset in d shows the FFT pattern of the wurtzite InN nanocolumn. (e) HRTEM lattice image of the area in d indicated by the red arrow.

Figure 3c–e shows a high-resolution TEM (HRTEM) image of the top of an InN nanocolumn along the $[\bar{1}120]$ direction of InN along with the corresponding FFT pattern and lattice image. The results indicate that no metallic In was present on the top of the InN nanocolumn, and the InN nanocolumns were single-phase hexagonal crystals with preferred orientations along the c -axis. As shown in Figure 3e, the InN surface is the (0002) plane of InN, and direct measurement based on the lattice image yielded a lattice parameter of $c = 5.7 \text{ \AA}$. These results are in good agreement with previously reported XRD results [27].

The compositional depth profile and binding energy of the InN nanocolumns grown at 520 °C were evaluated by XPS (Figure 4). Figure 4a shows the variation in the atomic ratios of silicon, carbon, nitrogen, indium, and oxygen along the etching direction from the atmosphere to the InN interface toward the InN/Si(111) interface. The layer structure of InN on nitrided Si(111) was clearly observed. The elemental concentrations of indium and nitrogen were slightly reduced in the layer moving in the etching direction. The carbon atomic concentration decreased rapidly after the initial etching

step and then remained nearly constant. Unintentional oxygen incorporation occurred because of the impurities remaining in the vacuum background, and a high concentration of oxygen was detected near the interface due to oxygen incorporation. Specht et al. [28] reported similar results InN grown via MBE. High concentration of oxygen was also probably caused by voids between the substrate and InN nanocolumns. These results are in good agreement with the TEM images. However, no diffraction spots corresponding to crystalline oxygen-related impurities (e.g., In oxide) were observed in the selected area electron diffraction patterns; thus, the oxygen might exist as impurities or point defects in the film. Furthermore, XPS indicated a low concentration of carbon on the surfaces of the InN nanocolumns, which may have originated from the TMIn precursor and/or adsorbed carbon. Iwao et al. [29] indicated that carbon was incorporated as a background element during the plasma-assisted metal–organic molecular beam epitaxy (PA-MOMBE) growth of InN, although the properties were improved due to they prefer to form the CO and/or CO₂ with oxygen atoms that have slightly high concentration. Oxygen contamination was previously reported in InN grown via RF-MOMBE [30].

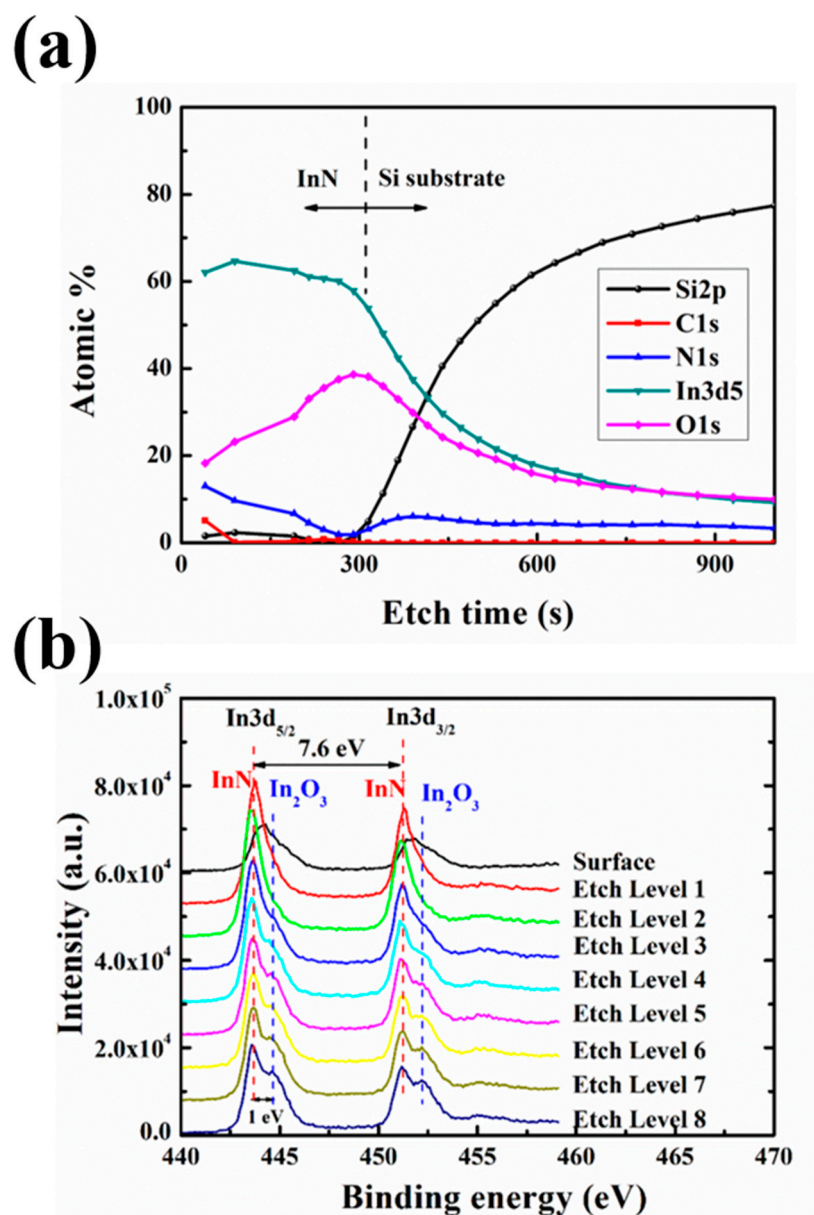


Figure 4. (a) XPS depth profile and (b) In3d spectra of InN nanocolumns grown on a nitrided Si(111) substrate at 520 °C.

Figure 4b shows the In3d XPS spectra of InN nanocolumns grown at 520 °C obtained from 440 to 458 eV at various depths of the film. Overlapping peaks were deconvoluted using XPSpeak41 software. Based on the XPS spectra, the binding energies (BEs) of In3d_{3/2} and In3d_{5/2} were determined to be 451.2 and 443.6 eV, respectively. This indicates that the difference in the BEs of the In3d_{3/2} and In3d_{5/2} spin-orbit doublet was almost constant at 7.6 eV with an intensity ratio of 4:3, in agreement with the literature [31]. The spectrum corresponding to the surface of the InN nanocolumn shows a broad peak at 444.2 eV and a shoulder peak at 444.6 eV, which are assigned to the BEs of In–N [32] and In₂O₃ (BE = 444.6–444.9 eV) [33], respectively. This may be related to the absorption of H₂O on the InN surface. Specht et al. [28] reported similar results for InN grown via MBE.

The Raman spectrum of the wurtzite InN nanocolumns on a nitrated Si(111) substrate (Figure 5) exhibits E₂(high) peaks at 489 and 590 cm⁻¹ for the A₁(LO) mode under 488 nm excitation. The Raman peak positions of the A₁(LO) and E₂(LO) modes of the InN nanocolumns in this study agree well with previously reported values, and the narrow linewidth is similar to that of high-quality InN films [34,35]. However, the strain-free Raman frequencies of the E₂(high) high and A₁(LO) modes of InN remain uncertain, and the reported values vary widely from 483 to 495 cm⁻¹ for the E₂(high) mode and 580–596 cm⁻¹ for the A₁(LO) mode [36].

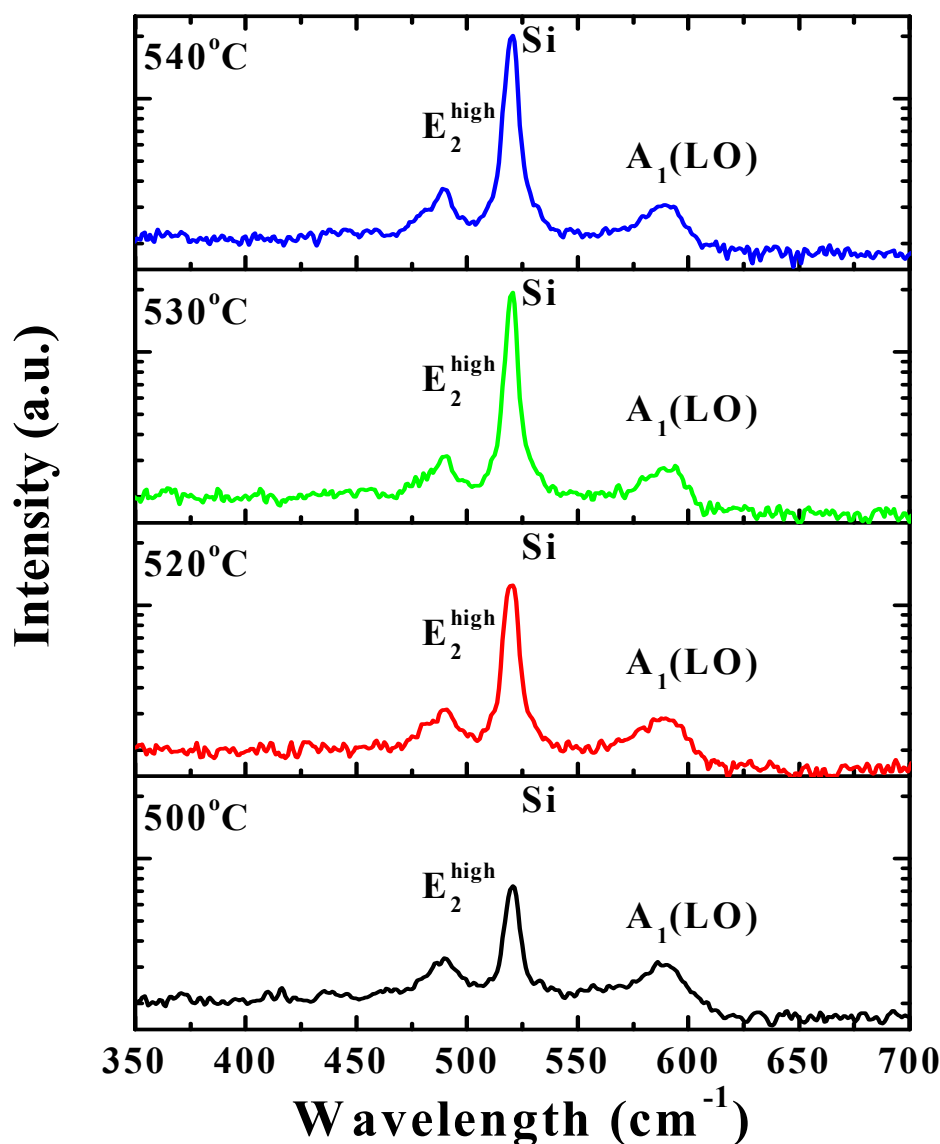


Figure 5. Room temperature Raman spectra of InN nanocolumns on a nitrated Si(111) substrate.

4. Conclusions

We fabricated hexagonal InN nanocolumns on nitrided Si(111) substrates via RF-MOMBE and studied the effect of growth temperature on the structural, morphological, optical, and compositional properties of the InN nanocolumns. The XRD results indicated that highly <0001>-oriented hexagonal InN nanocolumns were grown on the nitride Si(111) substrates. FESEM analysis demonstrated that the diameters of the InN nanocolumns on nitrided Si(111) depended strongly on the growth temperature. Hexagonal, pyramid-like 3D InN nanocolumns with high density were observed rather than one-dimensional InN nanowires. The Si₃N₄ buffer layer appeared to aid the self-assembly of the InN nanocolumns. The lattice parameter observed by HRTEM ($c = 5.7 \text{ \AA}$) agrees well with that of wurtzite-structured InN. The surface of the nitrided Si(111) substrate was clearly rough, likely as a result of damage from the RF plasma beam. The XPS results showed that oxygen was incorporated into the InN nanocolumns. The observation of the A₁(LO) and E₂(high) phonon modes of InN in the Raman spectrum confirmed the hexagonal structures of the InN nanocolumns. These findings indicate that the nitrided Si(111) substrate is essential for engineering the growth of InN on Si wafers. This substrate may also be applicable for other lattice-mismatched group-III–V heteroepitaxial systems. Nanocolumn structures containing heterojunctions could find applications in highly confined optoelectronic and electronic devices.

Author Contributions: W.-C.C. carried out most of the experimental work, including the preparation and characterization of InN nanocolumns and the drafting of the manuscript. T.-Y.Y. carried out the high-resolution XPS measurements. F.-I.L. and H.-P.C. supported the analysis of the InN samples. Y.-W.L. performed the XRD measurements. S.-Y.K. revised the manuscript. All authors read and approved the manuscript.

Funding: This research was funded by the Ministry of Science and Technology, grant number MOST 107-2111-E-492-001 and MOST 107-2622-E-492-012-CC3

Acknowledgments: The authors would like to thank L.L. Wei carried out the high-resolution TEM analysis.

Conflicts of Interest: The authors declare no conflicts of interest.

References

1. Bhuiyan, A.G.; Hashimoto, A.; Yamamoto, A. Indium nitride (InN): A review on growth, characterization, and properties. *J. Appl. Phys.* **2003**, *94*, 2779–2808. [\[CrossRef\]](#)
2. Wu, J. When group-III nitrides go infrared: New properties and perspectives. *J. Appl. Phys.* **2009**, *106*, 011101. [\[CrossRef\]](#)
3. Wu, J.; Walukiewicz, W.; Yu, K.M.; Ager, J.W.; Haller, E.E.; Lu, H.; Schaff, W.J.; Saito, Y.; Nanishi, Y. Unusual properties of the fundamental band gap of InN. *Appl. Phys. Lett.* **2002**, *80*, 3967–3969. [\[CrossRef\]](#)
4. Feneberg, M.; Däubler, J.; Thonke, K.; Sauer, R.; Schley, P.; Goldhahn, R. Mahan excitons in degenerate wurtzite InN: Photoluminescence spectroscopy and reflectivity measurements. *Phys. Rev. B* **2008**, *77*, 245207. [\[CrossRef\]](#)
5. Higashiwaki, M.; Matsui, T. Epitaxial growth of high-quality InN films on sapphire substrates by plasma-assisted molecular-beam epitaxy. *J. Cryst. Growth* **2003**, *252*, 128–135. [\[CrossRef\]](#)
6. Feng, S.; Tan, J.; Li, B.; Song, H.; Wu, Z.; Chen, X. Nitridation effects of Si(111) substrate surface on InN nanorods grown by plasma-assisted molecular beam epitaxy. *J. Alloys Compd.* **2015**, *621*, 232–237. [\[CrossRef\]](#)
7. Yamamoto, A.; Yamauchi, Y.; Ohkubo, M.; Hashimoto, A.; Saitoh, T. Heteroepitaxial growth of InN on Si(111) using a GaAs intermediate layer. *Solid State Electron.* **1997**, *41*, 149–154. [\[CrossRef\]](#)
8. Ahn, H.; Shen, C.H.; Wu, C.L.; Gwo, S. Spectroscopic ellipsometry study of wurtzite InN epitaxial films on Si(111) with varied carrier concentrations. *Appl. Phys. Lett.* **2005**, *86*, 201905. [\[CrossRef\]](#)
9. Kumar, M.; Rajpalke, M.K.; Bhat, T.N.; Roul, B.; Sinha, N.; Kalghatgi, A.T.; Krupanidhi, S.B. Growth of InN layers on Si(111) using ultra thin silicon nitride buffer layer by NPA-MBE. *Mater. Lett.* **2011**, *65*, 1396–1399. [\[CrossRef\]](#)
10. Pan, Y.; Wang, T.; Shen, K.; Peng, T.; Wu, K.; Zhang, W.; Liu, C. Rapid growth and characterization of InN nanocolumns on InGaN buffer layers at a low ratio of N/In. *J. Cryst. Growth* **2010**, *313*, 16–19. [\[CrossRef\]](#)

11. Gauckler, L.J.; Lukas, H.L.; Tien, T.Y. Crystal chemistry of β - Si_3N_4 solid solutions containing metal oxides. *Mater. Res. Bull.* **1976**, *11*, 503–512. [[CrossRef](#)]
12. Grandal, J.; Sánchez-García, M.A.; Calleja, E.; Gallardo, E.; Calleja, J.M.; Luna, E.; Trampert, A.; Jahn, A. InN nanocolumns grown by plasma-assisted molecular beam epitaxy on A-plane GaN templates. *Appl. Phys. Lett.* **2009**, *95*, 029901. [[CrossRef](#)]
13. Monteagudo-Lerma, L.; Valdueza-Felip, S.; Núñez-Cascajero, A.; Ruiz, A.; González-Herráez, M.; Monroy, E.; Naranjo, F.B. Morphology and arrangement of InN nanocolumns deposited by radio-frequency sputtering: Effect of the buffer layer. *J. Cryst. Growth* **2016**, *434*, 13–18. [[CrossRef](#)]
14. Yun, S.H.; Ra, Y.H.; Lee, Y.M.; Song, K.Y.; Cha, J.H.; Lim, H.C.; Kim, D.W.; Suthan Kissinger, N.J.; Lee, C.R. Growth of hexagonal and cubic InN nanowires using MOCVD with different growth temperatures. *J. Cryst. Growth* **2010**, *312*, 2201–2205. [[CrossRef](#)]
15. Kuo, S.Y.; Lai, F.-I.; Chen, W.C.; Hsiao, C.N. Catalyst-free growth and characterization of gallium nitride nanorods. *J. Cryst. Growth* **2008**, *310*, 5129–5133. [[CrossRef](#)]
16. Chen, W.C.; Kuo, S.Y.; Lai, F.-I.; Lin, W.T.; Hsiao, C.N. Effect of substrate temperature on structural and optical properties of InN epilayer grown on GaN template. *Thin Solid Films* **2013**, *529*, 169–172. [[CrossRef](#)]
17. Segura-Ruiz, J.; Garro, N.; Cantarero, A.; Denker, C.; Malindretos, J.; Rizzi, A. Optical studies of MBE-grown InN nanocolumns: Evidence of surface electron accumulation. *Phys. Rev. B* **2009**, *79*, 115305. [[CrossRef](#)]
18. Park, S.E.; Lim, S.M.; Lee, C.R.; Kim, C.S.; Byung-sung, O. Influence of SiN buffer layer in GaN epilayers. *J. Cryst. Growth* **2003**, *249*, 487–491. [[CrossRef](#)]
19. Nishikawa, S.; Nakao, Y.; Naoi, H.; Araki, T.; Nab, H.; Nanishi, Y. Growth of InN nanocolumns by RF-MBE. *J. Cryst. Growth* **2007**, *301–302*, 490–495. [[CrossRef](#)]
20. Grandal, J.; Sánchez-García, M.A.; Calleja, E. Accommodation mechanism of InN nanocolumns grown on Si (111) substrates by molecular beam epitaxy. *Appl. Phys. Lett.* **2007**, *91*, 021902. [[CrossRef](#)]
21. Lee, S.H.; Jang, E.S.; Kim, D.W.; Lee, I.H.; Navamathavan, R.; Kannappan, S.; Lee, C.R. InN nanocolumns grown on a Si(111) substrate using Au+In solid solution by metal organic chemical vapor deposition. *Jpn. J. Appl. Phys.* **2009**, *48*, 04C141-1–04C141-3. [[CrossRef](#)]
22. Tansley, T.L.; Foley, C.P. Optical band gap of indium nitride. *J. Appl. Phys.* **1986**, *59*, 3241–3244. [[CrossRef](#)]
23. Stoica, T.; Meijers, R.; Calarco, R.; Richter, T.; Lüth, H. MBE growth optimization of InN nanowires. *J. Cryst. Growth* **2006**, *290*, 241–247. [[CrossRef](#)]
24. Denker, C.; Malindretos, J.; Werner, F.; Limbach, F.; Schuhmann, H.; Niermann, T.; Seibt, M.; Rizzi, A. Self-organized growth of InN-nanocolumns on p-Si(111) by MBE. *Phys. Status Solidi C* **2008**, *5*, 1706–1708. [[CrossRef](#)]
25. Wu, C.-L.; Chen, W.-S.; Su, Y. N₂-plasma nitridation on Si(111): Its effect on crystalline silicon nitride growth. *Surf. Sci.* **2012**, *606*, L51–L54. [[CrossRef](#)]
26. Yamamoto, A.; Tsujino, M.; Ohkubo, M.; Hashimoto, A. Nitridation effects of substrate surface on the metalorganic chemical vapor deposition growth of InN on Si and α - Al_2O_3 substrates. *J. Cryst. Growth* **1994**, *137*, 415–420. [[CrossRef](#)]
27. Chen, W.-C.; Chen, H.-P.; Kuo, S.-Y.; Lai, F.I.; Hsiao, C.-N.; Lee, C.-C. Evaluation of the impact of T_{min} flow rate on the structural and optical properties of InN/ZnO heterojunctions using RF-MOMBE. *J. Cryst. Growth* **2017**, *475*, 88–92. [[CrossRef](#)]
28. Specht, P.; Armitage, R.; Ho, J.; Gunawan, E.; Yang, Q.; Xu, X.; Kisielowski, C.; Weber, E.R. The influence of structural properties on conductivity and luminescence of MBE grown InN. *J. Cryst. Growth* **2004**, *269*, 111–118. [[CrossRef](#)]
29. Iwao, K.; Yamamoto, A.; Hashimoto, A. Origins of n-type residual carriers in RF-MOMBE grown InN layers. *Phys. Status Solidi C* **2007**, *4*, 2453–2456. [[CrossRef](#)]
30. Chen, W.-C.; Tian, J.-S.; Wu, Y.H.; Wang, W.L.; Kuo, S.-Y.; Lai, F.I.; Chang, L. Influence of V/III Flow Ratio on Growth of InN on GaN by PA-MOMBE. *ECS J. Solid State Sci. Technol.* **2013**, *2*, P305–P310. [[CrossRef](#)]
31. Moulder, J.F.; Stickle, W.F.; Sobol, P.E.; Bomben, K.D. *Handbook of X-Ray Photoelectron Spectroscopy: A Reference Book of Standard Spectra for Identification and Interpretation of XPS Data*; Chastain, J., Ed.; Perkin-Elmer Corporation, Physical Electronics Division: Eden Prairie, MN, USA, 1992.
32. Parala, H.; Devi, A.; Hipler, F.; Maile, E.; Birkner, A.; Becker, H.W.; Fischer, R.A. Investigations on InN whiskers grown by chemical vapour deposition. *J. Cryst. Growth* **2001**, *231*, 68–74. [[CrossRef](#)]

33. Masuda, Y.; Kondo, M.; Koumoto, K. Site-selective deposition of In_2O_3 using a self-assembled monolayer. *Cryst. Growth Des.* **2009**, *9*, 555–561. [[CrossRef](#)]
34. Pu, X.D.; Chen, J.; Shen, W.Z.; Ogawa, H.; Guo, Q.X. Temperature dependence of Raman scattering in hexagonal indium nitride films. *J. Appl. Phys.* **2005**, *98*, 033527. [[CrossRef](#)]
35. Briot, O.; Maleyre, B.; Ruffenach, S.; Gil, B.; Piquier, C.; Demangeot, F.; Frandon, J. Absorption and Raman scattering processes in InN films and dots. *J. Cryst. Growth* **2004**, *269*, 22–28. [[CrossRef](#)]
36. Qian, Z.G.; Shen, W.Z.; Ogawa, H.; Guo, Q.X. Experimental studies of lattice dynamical properties in indium nitride. *J. Phys. Condens. Matter* **2004**, *16*, R381–R414. [[CrossRef](#)]



© 2019 by the authors. Licensee MDPI, Basel, Switzerland. This article is an open access article distributed under the terms and conditions of the Creative Commons Attribution (CC BY) license (<http://creativecommons.org/licenses/by/4.0/>).